Engineering 19 (2022) 199–206

Contents lists available at ScienceDirect

Engineering

journal homepage: www.elsevier.com/locate/eng

Research
Energy Batteries—Article

Ether-/Ester-/Fluorine-Rich Binding Emulsion Formula for Lithium-Ion Batteries

Xianqing Zeng [a,c], Donglin Han [a], Zeheng Li [c], Hongxun Wang [d], Gu Wu [c], Yong Deng [b], Kai Liu [b], Li Xie [b], Chengdu Liang [c], Min Ling [c,*], Yuchuan Huang [a,b,*]

[a] China Tobacco Sichuan Industrial Co., Ltd., Chengdu 610066, China
[b] Sichuan Sanlian New Material Co., Ltd., Chengdu 610041, China
[c] Key Laboratory of Biomass Chemical Engineering of the Ministry of Education, College of Chemical and Biological Engineering, Zhejiang University, Hangzhou 310027, China
[d] School of Metallurgy and Environment, Central South University, Changsha 410083, China

ARTICLE INFO

Article history:
Received 28 March 2020
Revised 10 May 2022
Accepted 20 May 2022
Available online 18 October 2022

Keywords:
Silicon anode
Emulsion copolymerization
Fluorine atom
Ether
Ester

ABSTRACT

Practical application of a Si anode in a high-energy-density battery cannot be achieved due to the huge volume expansion of these anodes. Researchers have focused on binders of the anode to restrict volume expansion in order to address this issue, as the hydrogen bonds and mechanical properties of binders can be used to enhance adhesion and accommodate the volume changes of a Si anode. Herein, we comprehensively consider binders' hydrogen bonds, mechanical properties, stability, and compatibility with the electrolyte solution, and design an ether-/ester-/fluorine-rich composite polymer, named P(TFEMA-*co*-IBVE). The proposed binder formula possesses outstanding stability, adhesion, and mechanical strength; moreover, it can accommodate the dramatic volume changes of a Si electrode and exhibits excellent electrochemical performance, achieving a high areal capacity of about 5.4 mA·h·cm^{-2}. This novel polymer design may be applied to other electrode materials in the next generation of lithium-ion batteries.

1. Introduction

Commercial graphite-based lithium-ion batteries (LIBs) cannot satisfy the high-energy-density demands of electric vehicles and smart grids [1–6]. Silicon (Si) is a promising candidate for building high-energy LIBs due to its energy-density capacity, which is ten times greater than that of graphite [7–11]. Nevertheless, practical applications of Si anodes are restricted by the volume expansion of such anodes (>300%) during repetitive lithiation and delithiation. Such a great volume expansion can lead to severe particle pulverization of Si anode materials and excessive growth of an unstable solid electrolyte interphase (SEI), resulting in drastic capacity fading. Researchers have conducted numerous studies to address the aforementioned issues [12,13]; for example, they have employed nanostructured or porous-structured Si-based materials [14–16] and synthesized composites of Si-based materials [17–20]. These efforts can improve the cycle performance of Si anodes to some extent, but usually lead to low initial coulombic efficiency (ICE) and small volumetric capacity.

Alternatively, employing high-quality electrode binders allow the anodes to effectively endure the volume change of Si and ensure the mechanical and electronic integrity of the electrode [21–23]. Polymer binders with functional groups (e.g., –COOH, –OH, and –NH_2)—such as sodium alginate (SA) [24,25], polyacrylic acid (PAA) [26–28], carboxymethyl cellulose (CMC) [29], guar gum [30], and polyvinyl alcohol (PVA) [31]—have been used to improve the interaction with silicon by forming hydrogen bonds between hydroxyl groups on the silicon surface and the carboxyl or hydroxyl groups of these binders. Some three-dimensional (3D) crosslinked polymers—such as CMC/PAA, PAA/polyaniline [32], poly(furfuryl alcohol)–PVA [33], and others [26,34]—have been explored as binders to improve the electrochemical performance of Si anodes. Crosslinked networks can cause chemical interactions between binder chains, endowing the chains with excellent mechanical properties. Recently, researchers have synthesized polymer binders by means of copolymerization. Gao et al. [35] prepared a tri-block copolymer (styrene-*b*-methyl

* Corresponding authors.
E-mail addresses: minling@zju.edu.cn (M. Ling), 245184914@qq.com (Y. Huang).

https://doi.org/10.1016/j.eng.2022.05.020

acrylate-*b*-styrene, SMAS) via reversible addition-fragmentation chain transfer emulsion polymerization and introduced an adhesion block (polystyrene) and elasticity block (methyl acrylate) into the polymer binder to improve the performance of a Si anode. Wang et al. [36] reported a rigid-soft modulated polymer binder, which accommodated the volume changes of a Si anode through multiple *in situ* self-healing network structures. Table S1 (Appendix A) lists the cycle performance of a Si anode with different binders [30–32,35–43]. In fact, these binders, which were attempted in order to address the issues of Si anodes, still mostly depend on hydrogen bonds and on controlling the mechanical properties. Although the use of functional groups and network structures improve the electrochemical performance of the Si anode, most of these procedures are too complicated to scale up and are generally unable to achieve high mass loading and long-cycling stability.

Poly(vinylidene fluoride) (PVDF) is a conventional binder used in traditional LIBs. Can it also be used as a commercial binder for Si anodes? PVDF polymers possess suitable adhesion and extremely high chemical and thermal stability, due to the special fluorine atom. Herein, inspired by PVDF and the strategy described above, we report on our design of an ether-/ester-/fluorine-rich comprehensive polymer synthesized by the emulsion copolymerization of trifluoroethyl methacrylate (TFEMA) and isobutyl vinyl ether (IBVE) monomers, denoted as P(TFEMA-*co*-IBVE). Introducing fluorine into the polymer skeleton can introduce thermostability, inoxidizability, and chemical inertness into the binder [44,45]—features that can robustly enhance the binder's stability. Moreover, the strong polarity of fluorine can produce a high and cohesive energy density, resulting in mechanical strength. Furthermore, vinyl ether (VE) has been widely used in the adhesive industry [46,47], probably because the active and polar oxygen atoms in poly(vinyl ether) polymers can interact with other substances [36,48]. The rotatable carbon–oxygen single bond endows the polymer with a low glass transition temperature and good flexibility, which balances with the mechanical stiffness to allow the polymer to tolerate the large volume expansion of the Si anode [49,50]. As ester bonds are compatible with carbonate electrolyte solutions, their inclusion in the binder can improve the electrode's wettability to the electrolyte and facilitate Li-ion diffusion. The carbonyl group can also form hydrogen bonds at the interface [51]. Based on these advantages, the proposed P(TFEMA-*co*-IBVE)-based Si anode can accommodate dramatic volume changes while exhibiting stability and high adhesive properties, resulting in better cycling and an improved rate performance, especially under high areal capacities.

2. Material and methods

2.1. Materials

IBVE (99.5%), CMC, poly(1,1-difluoroethylene) (PVDF), sodium dodecyl sulfate (SDS), potassium persulfate (KPS), and sodium sulfite ($NaHSO_3$) were purchased from Aladdin Industrial Co., Ltd. (USA), without extra purification before use. TFEMA (98%) and OP-10 emulsifier were purchased from Shanghai Macklin Biochemical Co., Ltd. (China), without extra purification. Si powder was purchased from Hai Tian Company (China). Electrolyte and fluoroethylene carbonate (FEC) were purchased from Enli New Energy Technology Co., Ltd. (China).

2.2. Preparation of the P(TFEMA-co-IBVE) copolymer

First, 0.1 g of emulsifier (SDS/OP-10) was dissolved in 10 g of deionized water in a 250 mL flask, and the hydrophile–lipophile balance (HLB) value was adjusted to 10. Then, 1 g of TFEMA and 3 g of IBVE were added to the solution, followed by 30 min of deoxygenation via nitrogen purging. Next, 0.02 g of a mixture of the initiators (KPS and $NaHSO_3$, mixed in a 2:1 ratio) was added to the flask. The temperature of the water bath was raised to 60 °C to start emulsion polymerization. After 1 h, another 1 g of TFEMA and the remaining 0.02 g of the initiator mixture were injected over an additional 3 h to complete the polymerization. Finally, an emulsion of P(TFEMA-*co*-IBVE) with a solid content of about 20 wt% was obtained. After resting for 1 month, the emulsion had no delamination. Mass ratios of TFEMA and IBVE in different polymer samples were set at 3:7, 4:6, and 5:5, respectively, to optimize the copolymer; these samples were denoted as P(3TFEMA-*co*-7IBVE), P(4TFEMA-*co*-6IBVE), and P(5TFEMA-*co*-5IBVE), respectively. The same procedure was used to synthesize the poly(TFEMA) (P(TFEMA)) emulsion and poly(IBVE) (P(IBVE)) emulsion, except that no IBVE monomer and no TFEMA monomer were added, respectively.

2.3. Preparation of electrodes

Emulsions of P(TFEMA-*co*-IBVE) with different monomer ratios were directly used as binders after adding CMC (a thickener); the weight ratio of P(TFEMA-*co*-IBVE):CMC was 1:1. For the purpose of comparison, aqueous CMC and organic PVDF were used as control binders. The electrodes were typically prepared by mixing nano-Si particles, Super P conductive carbon, and binder with a mass ratio of 7:2:1 in solvent to form a homogeneous slurry on copper foil. After drying in a vacuum at 100 °C over night P(3TFEMA-*co*-7IBVE)-based, P(4TFEMA-*co*-6IBVE)-based, P(5TFEMA-*co*-5IBVE)-based, CMC-based, and PVDF-based Si electrodes were obtained. Finally, the electrode films were cut into small disks with a diameter of 12 mm. The mass loadings were all about 1.0 mg·cm^{-2}, except as otherwise noted. The same operations were adopted for the active materials of Si/C anodes.

2.4. Materials characterization

Number-average molecular weight (M_n) and weight-average molecular weight (M_w) were measured by means of gel permeation chromatography (GPC) using a PL-GPC 50 Plus (tetrahydrofuran (THF), 25 °C; Varian, USA). Nuclear magnetic resonance (NMR) was tested on 600 MHz DD2 (DirectDrive2, $CDCl_3$, 25 °C, tetramethylsilane; Agilent Technologies, USA). Fourier-transform infrared (FTIR) spectra were recorded using an FTIR analyzer (THF, 25 °C; Nicolet 5700, Thermo Fisher Scientific, USA). Scanning electron microscopy (SEM) was performed with a Hitachi S-4800 scanning electron microscope (Japan). Energy dispersive X-ray spectroscopy (EDS) was performed with a spectroscope attached to the scanning electron microscope. Transmission electron microscopy (TEM) was collected with a HT-7700 field-emission transmission electron microscope (Hitachi). Differential scanning calorimetry (DSC) measurements were performed using a DSC 204HP instrument (25 °C; NETZSCH, Germany). Contact angle (CA) testing was conducted using a CA measuring device (OCA 20, 25 °C; DataPhysics Instruments GmbH, Germany) with a $LiPF_6$/ethylene carbonate (EC)/diethyl carbonate (DEC) electrolyte dropping on the Si electrodes at room temperature.

Adhesive measurement of Raman spectra was performed using a LabRAM HR Evolution Raman spectrometer system (25 °C; Horiba Jobin Yvon, USA) with an excitation wavelength of 532 nm. The mixed electrodes were prepared using the same procedure as described above for the silicon electrodes; afterward, a stress of 10 MPa was applied to the electrodes. Then, the ground electrodes were baked at 100 °C for 6 h. Later, the baked electrodes were soaked in the $LiPF_6$/EC/DEC electrolyte at room temperature for 6 h.

The peeling test was performed using a ZwickRoell Z020 (25 °C; Germany). The Si electrodes, which had been prepared as described above, were cut into rectangular strips of 6 cm with a width of 2 cm. Copper foil side of the rectangular eletrode was stuck onto the slide with 3M double-sided adhesive tape, and the other side coated with Si mixed slurry, attached with single-sided adhesive tape. Fix one end of the slide and one end of the single-sided adhesive tape, then peel 180° from the opposite direction at a speed of 50 mm·min^{-1}. To ensure the accuracy of the test results, each sample was tested 3–5 times.

A swelling test was used to measure the compatibility of the binder with the electrolyte solvent. The binders were placed in the $LiPF_6$/EC/DEC electrolyte at room temperature for 48 h, and the swelling ratio was calculated by the weight ratio of the amount of absorbed solvent to the weight before soaking.

2.5. Electrochemical measurements

Electrochemical tests were assembled and performed using CR2025-type coin cells in an argon (Ar)-filled glovebox. Lithium (Li) metal foil was utilized as the counter electrode, Celgard 2400 was used as the separator, and the electrolyte consisted of 1.2 mol of $LiPF_6$ in a mixture of EC and DEC (1:1 in volume) and FEC (25 vol%). Galvanostatic charge–discharge measurements were conducted at a voltage ranging from 0.01 to 1.00 V with the LAND battery cycler test system (China). Current density and specific capacity were calculated based on the mass of the Si or Si/C active material.

3. Results and discussion

The synthesis of P(TFEMA-*co*-IBVE) is shown in Fig. 1(a). NMR was used to identify the molecular structure and composition of the copolymer. The different hydrogen atoms are labeled as a to j in Fig. 1(a). The ^{1}H NMR spectra ranged from −1 to 8 ppm, as shown in Fig. 1(b). The characteristic peaks of $-CH_3$, $-CH_2$, and –CH are located in the range of 0.8–2.1 ppm. The 2.7–3.5 ppm signal corresponds to the $-O-CH_2$ and –O–CH groups. The 4.4–4.8 ppm signal corresponds to $-CH_2-CF_3$. Fig. 1(c) displays the ^{19}F NMR spectrum; the signal at −73.3 ppm indicates the presence of the $-CF_3$ group. Based on the intensity of the peaks, we calculated the ratio of the two monomer units in the copolymer by integrating the ^{1}H NMR spectra using MestReNova software [52]. The monomer unit molar ratio of the IBVE monomer was 29.4% and that of the TFEMA monomer was 70.6% for the copolymer P(4TFEMA-*co*-6IBVE).

In addition to the NMR spectrum, we conducted FTIR to confirm the chemical structure of the P(TFEMA-*co*-IBVE) polymer, as shown in Fig. 2(a). IBVE and TFEMA were homopolymerized separately for comparison. The spectrum of P(IBVE) in blue shows a broad absorption band at 2923 cm^{-1}, which is ascribed to the stretching of C–H, and the peak at 1128 cm^{-1} is attributed to the stretching of the C–O–C bonds. The absorption peak at 2360 cm^{-1} is due to the interference of carbon dioxide. The spectrum of P(TFEMA) in black also shows an absorption band at 2923 cm^{-1}, which is ascribed to the stretching of C–H. The absorption peak at 1747 cm^{-1} is attributed to the stretching of the C=O group, and the peak at 1413 cm^{-1} comes from the C–H bond of $-CH_3$. The absorption peak at 1282 cm^{-1} comes from the C–F bond of $-CF_3$. The peak at 1130 cm^{-1} is ascribed to the stretching of the C–O bond. The characteristic peaks of an ether and an ester both appear in the green spectrum of P(TFEMA-*co*-IBVE). A shift in the C=O stretching and an enhancement of C–O are also observed, due to the copolymerization.

Subsequently, the number-average molecular weight (M_n) and mass-average molar mass (M_w) of the proposed P(TFEMA-*co*-IBVE) binder were measured using GPC. The revealed M_n and M_w were 278 000 and 718 000, respectively. The polydispersity (PDI) was calculated to be 2.58. The value of M_w and M_n meet the requirements for binder application in batteries [53,54]. In addition, the glass transition temperature (T_g) of the P(TFEMA-*co*-IBVE) copolymer is 51.8 °C (Fig. S1 in Appendix A), which is much smaller than those of highly crystallized binders. The suitable T_g bestows the copolymer with mechanical stiffness and elasticity, which are beneficial for tolerating the volume variations in the silicon electrode during cycling. The morphology and microstructure

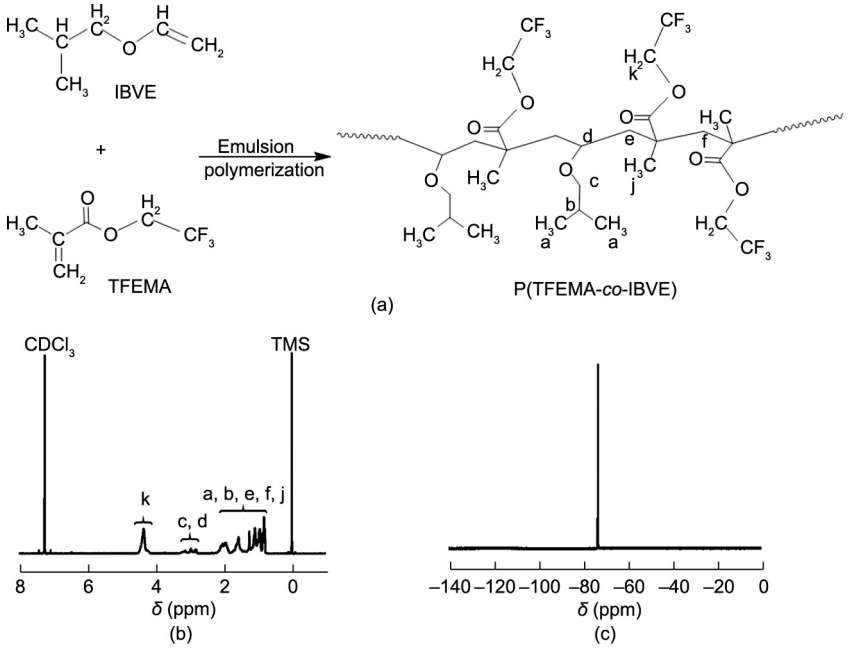

Fig. 1. (a) Reaction equation of the emulsion polymerization and structural formulas of the reactants and product; (b) ^{1}H NMR spectrum of the obtained P(TFEMA-*co*-IBVE) polymer (TMS: tetramethylsilane; δ: chemical shift); (c) ^{19}F NMR spectrum of the P(TFEMA-*co*-IBVE) copolymer.

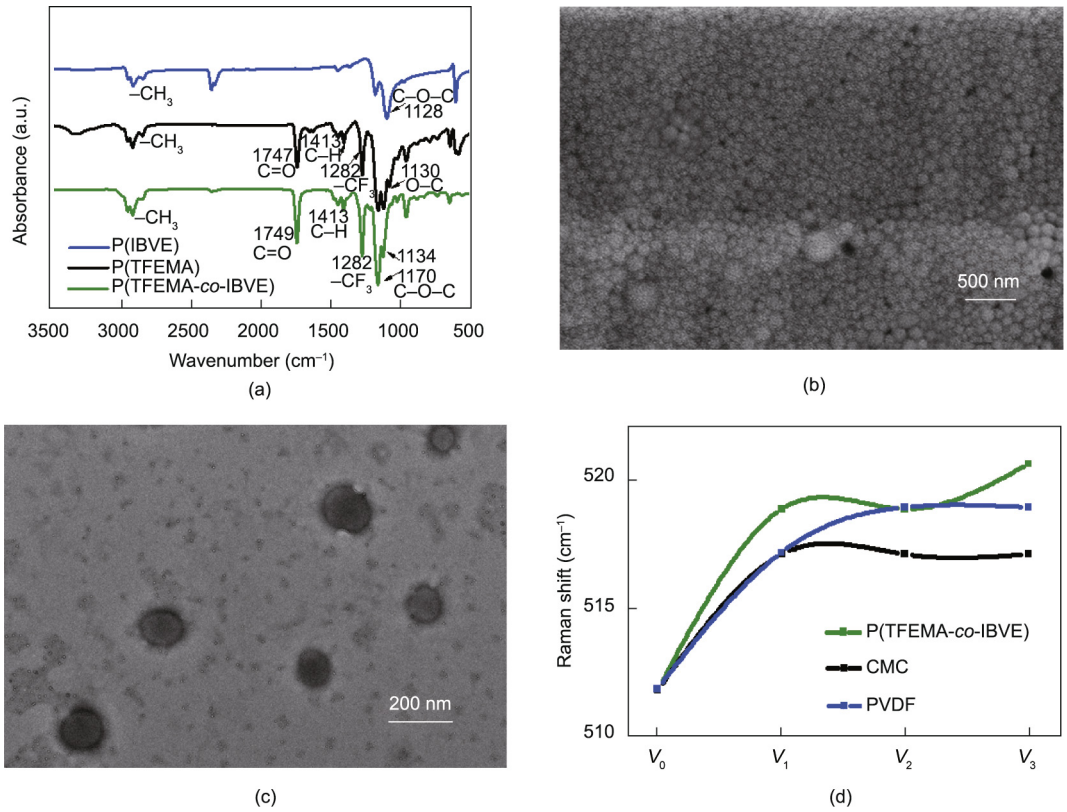

Fig. 2. (a) FTIR spectra of P(TFEMA-*co*-IBVE), P(TFEMA), and P(IBVE); (b) SEM and (c) TEM images of the obtained emulsion polymerization copolymer; (d) Raman shift of silicon with P(TFEMA-*co*-IBVE), CMC, and PVDF in a different state. a.u.: absorbance unit.

of the latex particles were also monitored using SEM and TEM. The emulsion consists of thousands of uniformly distributed spherical latex particles, as shown in Fig. 2(b); the TEM images reveal that the diameters of the latex particles (dyed with uranyl acetate) are 100–150 nm (Fig. 2(c)). The corresponding EDS spectrum elemental map of the spherical latex particles shows the presence of C, O, and F in the copolymer, as shown in Fig. S2 in Appendix A. These images and mappings indicated the realization of ether-/ester-/fluorine-rich spherical latex particles.

To evaluate the stability and strong adhesiveness of the composite binder, we performed a Raman spectroscopy analysis of the P(TFEMA-*co*-IBVE) binder combined with Raman-active silicon. This test method is nondestructive and closer to the practical conditions of a LIB. CMC and PVDF binders were also evaluated as references. As shown in Fig. 2(d), the point corresponding to V_0 represents pure Si particles, and the characteristic Raman shift is 511.88 cm^{-1}. When pressure was applied to the mixed electrodes (see the experiment section for a detailed procedure), the silicon remained compressed, being affected by the adhesive, and the Raman shift (marked as V_1) increased. The higher the adhesive strength, the larger the Raman shift [55]; it is clear that the Raman shift of the P(TFEMA-*co*-IBVE) (green line) changed more than those of the CMC (black line) and PVDF (blue line). Furthermore, the compressed electrodes were baked at a high temperature and soaked in the electrolyte to simulate the real environment of a Si electrode in a LIB. The Raman shift values of the baked and soaked electrodes are marked as V_2 and V_3, respectively (Fig. S3 in Appendix A shows the original Raman spectra). For the CMC-based and PVDF-based electrodes, after high temperature baking and immersion, the deformation of the silicon was recovered to a certain extent, and the Raman shift was reduced. In contrast, for the P(TFEMA-*co*-IBVE)-based electrode, the deformation of the silicon was maintained after soaking in the electrolyte, and the Raman shift even increased, as shown by the green point at V_3. This phenomenon indicates that the P(TFEMA-*co*-IBVE) composite binder exhibits a strong adhesive strength for silicon and possesses thermal and chemical stability, especially in a battery environment.

To further study the adhesive strength of the binders to the Si electrode, a peeling test was performed. Fig. S4(a) in Appendix A shows the peeling strength curves of the P(TFEMA-*co*-IBVE)-based, CMC-based, and PVDF-based Si electrodes. It can be seen from the figure that the peeling strength of the P(TFEMA-*co*-IBVE)-based Si electrode is about 4.5 N on average, while that of the CMC-based electrode is about 2 N and that of the PVDF-based electrode is only about 1 N. As shown in Fig. S4(b) in Appendix A, a large amount of powder peeled off from the CMC-based and PVDF-based Si electrode plates, while only a small quantity of particles peeled off from the P(TFEMA-*co*-IBVE)-based Si electrode plate. This result shows that the P(TFEMA-*co*-IBVE) binder has better adhesion to the silicon and can effectively fix the active material and conducting agent to the collector tightly, maintaining a more stable electrode structure.

Aside from adhesive strength and stability, a CA test was conducted to investigate the wettability and permeability properties of the binder in the electrolyte (Fig. 3). The diffusion properties are relevant to the binding strength, according to the diffusion theory [36]. As shown in Figs. 3(a) and (b), the P(TFEMA-*co*-IBVE)-based Si electrode initially exhibits a smaller CA (10.8°) than the CMC-based Si electrode (23.8°). Over time, the electrolyte stretches out on the Si electrode, and the P(TFEMA-*co*-IBVE)-based Si electrode still has a smaller CA in comparison with the CMC-based Si electrode. This result indicates that the P(TFEMA-*co*-IBVE) binder has a better wettability to the electrolyte, which will facilitate Li-ion diffusion within the electrode. This good wettability is

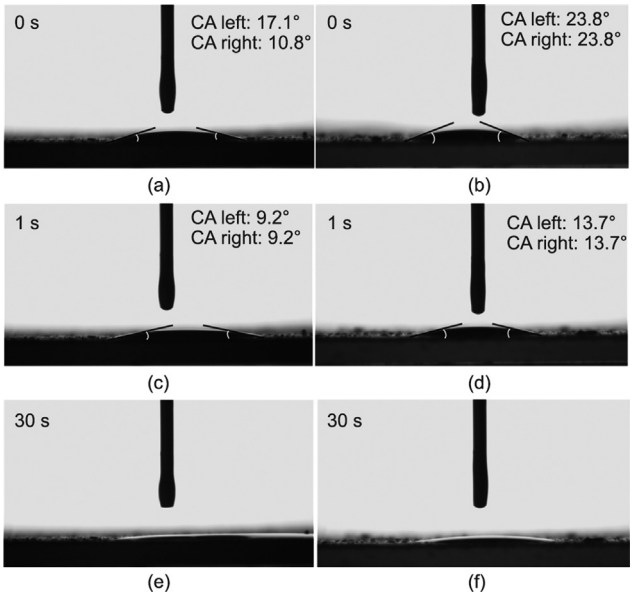

Fig. 3. CA test of the $LiPF_6$/EC/DEC electrolyte dropped on (a, c, e) the P(TFEMA-*co*-IBVE)-based Si electrode and (b, d, f) the CMC-based Si electrode.

probably because the P(TFEMA-*co*-IBVE) copolymer contains the same ester functional groups as the DEC and EC in the electrolyte; thus, according to the principle of similarity compatibility, the existence of ester functional groups in the P(TFEMA-*co*-IBVE) copolymer cause the polymer to be compatible with the carbonate electrolyte. Since PVDF is soluble in organic solvents, while P(TFEMA-*co*-IBVE) and CMC are water soluble, the organic-based PVDF is not considered to be part of the same system as the water-based binder, and its wettability with the electrolyte is not compared here.

In regard to the binder's swelling in the electrolyte, Fig. S5 in Appendix A shows that, in the P(TFEMA-*co*-IBVE) binder system, the electrolyte uptake is about 59% of its final weight in 48 h, which is higher than those of the CMC (28%) and PVDF (33%) binders. This high electrolyte uptake indicates that the P(TFEMA-*co*-IBVE) binder can help to accelerate the Li-ion transportation of the Si anode. In some sense, excellent ion diffusion also reflects favorable electrode kinetics, as it accelerates Li-ion transportation and improves the rate performance of the Si anode.

The effect of the composite binder on the galvanostatic charge–discharge was investigated. Silicon nanoparticles with diameters ranging from 50 to 100 nm were applied as the anode active material for this study (Fig. S6(a) in Appendix A). When combined with the P(TFEMA-*co*-IBVE) binder, the silicon particles were lightly enveloped and uniformly coated, as shown in Fig. S6(b) in Appendix A, ensuring a complete connection between the particles. As shown in Fig. S7 in Appendix A, the different binders used for the Si anodes—namely, P(3TFEMA-*co*-7IBVE), P(4TFEMA-*co*-6IBVE), and P(5TFEMA-*co*-5IBVE)—exhibited varying specific capacities. Among the Si anodes, the P(4TFEMA-*co*-6IBVE)-based Si anode showed the best cycling performance. Therefore, we chose P(4TFEMA-*co*-6IBVE) as the optimized copolymer for the Si anodes. This strategy was adopted in this paper; from this point on, all use of the term "P(TFEMA-*co*-IBVE)" refers to this ratio. Fig. 4(a) displays the voltage profiles of the P(TFEMA-*co*-IBVE)-based silicon electrode for the first, third, and tenth cycles. The cycle lithiation potential had a plateau profile at 0.10–0.01 V, which is consistent

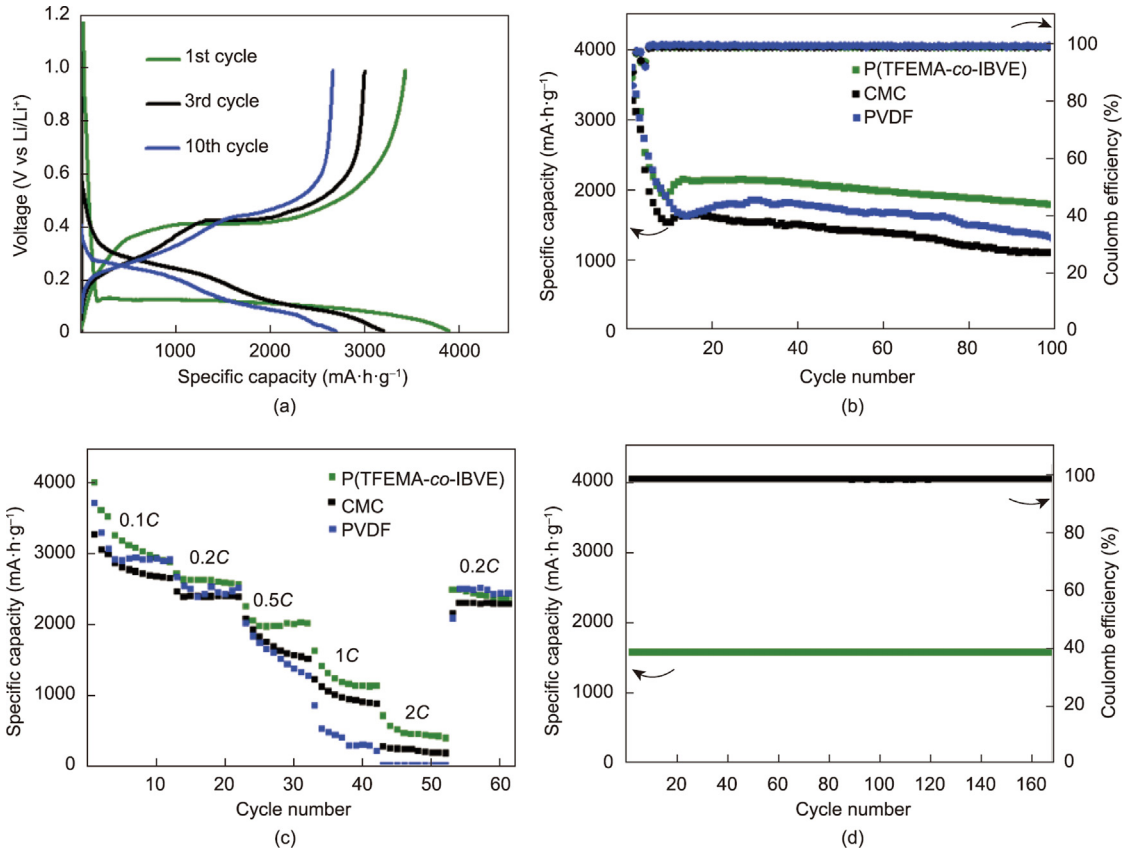

Fig. 4. (a) Charge/discharge voltage profiles of the P(TFEMA-*co*-IBVE)-based Si electrode; (b) cycle performance and coulombic efficiency of the P(TFEMA-*co*-IBVE)-based, CMC-based, and PVDF-based Si electrodes at 0.5*C*; (c) rate performance of the P(TFEMA-*co*-IBVE)-based, CMC-based, and PVDF-based Si electrodes; (d) cycle performance of the P(TFEMA-*co*-IBVE)-based Si electrode with a capacity limitation of 1600 mA·h·g^{-1}.

with the behavior of crystalline Si. The first discharge and charge capacities were 3884 and 3442 mA·h·g^{-1}, respectively, with a remarkable coulombic efficiency of 88.6%. The cycling stability and coulombic efficiency at 0.5*C* are shown in Fig. 4(b). It is noticeable that the P(TFEMA-*co*-IBVE)-based Si electrode shows a high specific capacity of 1811 mA·h·g^{-1} after 100 cycles, which is much higher than those of the CMC-based Si electrode (1120 mA·h·g^{-1} after 100 cycles) and PVDF-based Si electrode (1309 mA·h·g^{-1} after 100 cycles). Fig. 4(c) displays the rate performance. The P(TFEMA-*co*-IBVE)-based Si electrode retained its stable cycling stability at various rates of 0.1*C*, 0.2*C*, 0.5*C*, 1*C*, and 2*C*. When the current was changed back to 0.2*C*, the capacity reversibly returned to 2309 mA·h·g^{-1}. As shown in Fig. 4(d), the P(TFEMA-*co*-IBVE)-based Si electrode demonstrated extreme cycling stability after 160 cycles with the Li insertion (discharge) capacity being limited at 1600 mA·h·g^{-1} at 0.8 A·g^{-1}. Moreover, the average coulombic efficiency of a capacity-limited Si electrode after 160 cycles is 99.27%, showing a stable charge–discharge process. More significantly, the long-term cycling of the Si anode was evaluated at a current rate of 0.2*C* (Fig. S8 in Appendix A). After 300 continuous cycles, the electrode still maintained a discharge capacity of 1200 mA·h·g^{-1}. This excellent cycling performance is mainly due to the strong adhesive strength and mechanical properties of the P(TFEMA-*co*-IBVE) binder, which can maintain the integrity of the electrode even when the Si volume changes.

According to electrochemical impedance spectroscopy, as shown in Fig. 5(a), the charge-transfer impedance of the P(TFEMA-*co*-IBVE)-based Si electrode before cycling is lower than those of the CMC-based and PVDF-based electrodes, indicating that the electrode reaction kinetics inside the P(TFEMA-*co*-IBVE)-based Si electrode are faster. After charge–discharge cycling, it can be seen from Fig. 5(b) that the P(TFEMA-*co*-IBVE)-based Si electrode exhibits a lower electrochemical impedance than either of the CMC-based and PVDF-based electrodes. This is due to the good wettability of the P(TFEMA-*co*-IBVE) binder and electrolyte. Moreover, the P(TFEMA-*co*-IBVE) binder allows the active substance to come into sufficient contact with the conductive agent and the electrolyte, and makes it possible to maintain the structural stability of the electrode during the charge–discharge process.

In fact, the effectiveness of the proposed binder is best revealed when under industrial mass loading. In practical applications, a high areal capacity with a high mass loading is necessary yet difficult to achieve, especially for silicon-based anodes. A traditional binder system cannot deal with the ensuing volume expansion under such a high mass loading. Here, the P(TFEMA-*co*-IBVE)-based Si electrode exhibits a remarkable performance under a high mass loading. Fig. 5(c) shows the voltage profiles of the P(TFEMA-*co*-IBVE)-based Si electrode under a high loading for the first, third, and tenth charge–discharge cycles. The cycle lithiation potential has a plateau profile at 0.10–0.01 V. Fig. 5(d) and Fig. S9 in Appendix A show that the P(TFEMA-*co*-IBVE)-based Si electrode approaches an areal capacity of 5.4 mA·h·cm^{-2} and a specific capacity of 2070 mA·h·g^{-1}, which far exceed those of the CMC-based Si electrode (areal capacity: 2.1 mA·h·cm^{-2}) and the PVDF-based Si electrode (areal capacity: 4.48 mA·h·cm^{-2}). We also applied the two different binders to Si/C anodes. As shown in Fig. S10(a) in Appendix A, the P(TFEMA-*co*-IBVE)-based Si/C electrode clearly showed superior specific capacities in comparison with the CMC-based and PVDF-based Si/C electrodes at a rate of 0.2*C*. In particular, at the high rate of 1*C*, the P(TFEMA-*co*-IBVE)

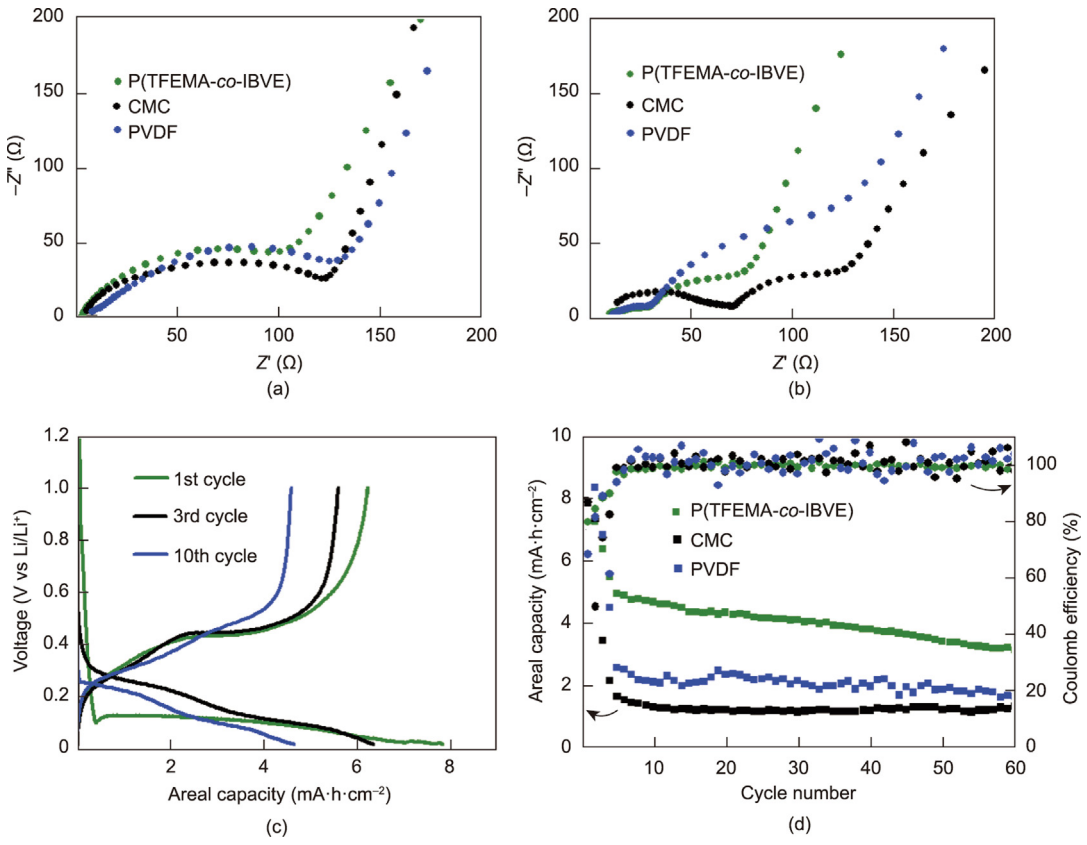

Fig. 5. (a, b) Electrochemical impedance spectroscopy of P(TFEMA-*co*-IBVE)-based, CMC-based, and PVDF-based Si electrodes (a) before and (b) after 20 cycles; (c) voltage profiles of a P(TFEMA-*co*-IBVE)-based Si electrode with a high mass loading; (d) areal capacity of Si anodes with a high Si mass loading of 3.2 mg·cm^{-2} at 0.1*C* of P(TFEMA-*co*-IBVE)-based, CMC-based, and PVDF-based Si electrodes.

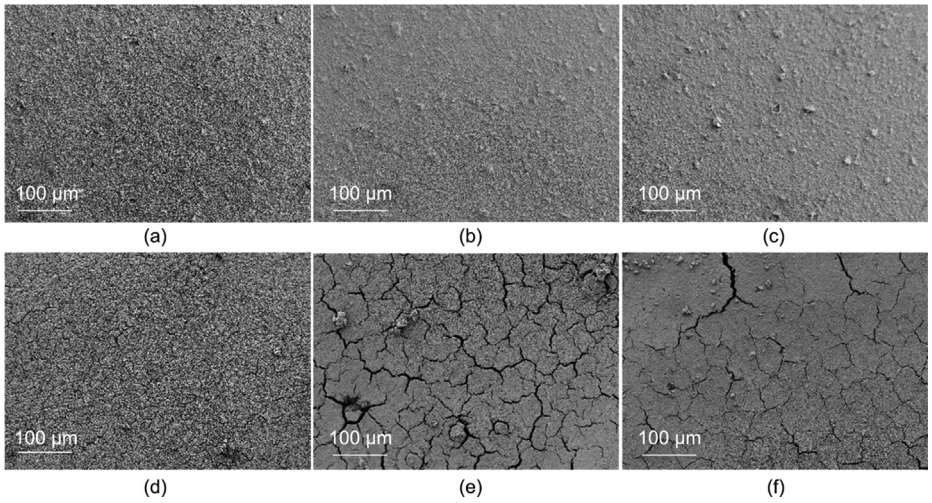

Fig. 6. (a–c) SEM images of (a) a P(TFEMA-*co*-IBVE)-based Si electrode, (b) CMC-based Si electrode, and (c) PVDF-based Si electrode; (d–f) SEM images of (d) a P(TFEMA-*co*-IBVE)-based Si electrode, (e) CMC-based Si electrode, and (f) PVDF-based Si electrode after 100 cycles.

binder exhibits a more significant advantage in terms of specific capacities (Fig. S10(b) in Appendix A). The results indicate that the P(TFEMA-*co*-IBVE) binder containing fluorine, ester, and ether groups contributes to the electrochemical stability of the electrode.

To further understand the improved electrochemical performance achieved by the P(TFEMA-*co*-IBVE) binder, we conducted SEM to characterize the surface morphologies of the Si electrode before and after cycling. Figs. 6(a)–(c) show the morphology of the pristine P(TFEMA-*co*-IBVE)-based, CMC-based, and PVDF-based Si electrodes, respectively. As shown in Fig. 6(d), there is no obviously detectable morphology change or microstructure destruction even after 100 cycles; rather, the structure of the P(TFEMA-*co*-IBVE)-based electrode is well preserved (see inset of Fig. S11 in Appendix A). In contrast, as shown in Figs. 6(e) and (f), the PVDF-based electrode shows severe cracks after 100 cycles, and the CMC-based electrode shows even worse cracking. The SEI layers on the silicon particles with the P(TFEMA-*co*-IBVE) binder is are believed to be thinner and more stable than those on the CMC and PVDF binders, indicating better electrode integrity.

4. Conclusions

In conclusion, we have synthesized a comprehensive copolymer binder via emulsion polymerization for use in battery applications. The fluorine, ester bond, and ether groups on the side chains of the polymers can not only enhance the adhesion but also improve the stability, mechanical strength, and wettability. This designed binder can effectively accommodate the large volume change of a silicon anode (ca. 300 vol%) on an industrial scale. Moreover, it exhibits excellent cycling stability, especially under a high mass loading. The composite binder achieves a high areal capacity of 5.4 $mA{\cdot}h{\cdot}cm^{-2}$, which reaches the industrial standard. The strategies proposed in this study improve the electrochemical performance of silicon anodes and establish a new strategy for the design of binders for other energy-storage devices.

Acknowledgments

This study was supported by funding from the National Key Research and Development Program of China (2018YFB0104300) and the Key Project of the Sichuan Science and Technology Department (2018GZ0546).

Compliance with ethics guidelines

Xianqing Zeng, Donglin Han, Zeheng Li, Hongxun Wang, Gu Wu, Yong Deng, Kai Liu, Li Xie, Chengdu Liang, Min Ling, and Yuchuan Huang declare that they have no conflict of interest or financial conflicts to disclose.

Appendix A. Supplementary data

Supplementary data to this article can be found online at https://doi.org/10.1016/j.eng.2022.05.020.

References

[1] Hu L, Wu H, La Mantia F, Yang Y, Cui Y. Thin, flexible secondary Li-ion paper batteries. ACS Nano 2010;4(10):5843–8.
[2] Li M, Lu J, Chen Z, Amine K. 30 years of lithium-ion batteries. Adv Mater 2018;30(33):1800561.
[3] Liu T, Zhang Y, Jiang Z, Zeng X, Ji J, Li Z, et al. Exploring competitive features of stationary sodium ion batteries for electrochemical energy storage. Energy Environ Sci 2019;12(5):1512–33.
[4] Zeng X, Gao X, Li G, Sun M, Lin Z, Ling M, et al. Conductive molybdenum carbide as the polysulfide reservoir for lithium–sulfur batteries. J Mater Chem A 2018;6(35):17142–7.
[5] Shen Y, Zhang J, Pu Y, Wang H, Wang B, Qian J, et al. Effective chemical prelithiation strategy for building a silicon/sulfur Li-ion battery. ACS Energy Lett 2019;4(7):1717–24.
[6] Song Z, Zhang G, Deng X, Zou K, Xiao X, Momen R, et al. Ultra-low-dose pre-metallation strategy served for commercial metal-ion capacitors. Nano-Micro Lett 2022;14(1):53.
[7] Erk C, Brezesinski T, Sommer H, Schneider R, Janek J. Toward silicon anodes for next-generation lithium ion batteries: a comparative performance study of various polymer binders and silicon nanopowders. ACS Appl Mater Interfaces 2013;5(15):7299–307.
[8] Zhao Y, Wang J, He Q, Shi J, Zhang Z, Men X, et al. Li-ions transport promoting and highly stable solid–electrolyte interface on Si in multilayer Si/C through thickness control. ACS Nano 2019;13(5):5602–10.
[9] Jin Y, Zhu B, Lu Z, Liu N, Zhu J. Challenges and recent progress in the development of Si anodes for lithium-ion battery. Adv Energy Mater 2017;7(23):1700715.
[10] Kim H, Han B, Choo J, Cho J. Three-dimensional porous silicon particles for use in high-performance lithium secondary batteries. Angew Chem Int Ed Engl 2008;47(52):10151–4.
[11] Devic T, Lestriez B, Roué L. Silicon electrodes for Li-ion batteries. Addressing the challenges through coordination chemistry. ACS Energy Lett 2019;4(2):550–7.
[12] Luo W, Chen X, Xia Y, Chen M, Wang L, Wang Q, et al. Surface and interface engineering of silicon-based anode materials for lithium-ion batteries. Adv Energy Mater 2017;7(24):1701083.
[13] Ling M, Zhao H, Xiao X, Shi F, Wu M, Qiu J, et al. Low cost and environmentally benign crack-blocking structures for long life and high power Si electrodes in lithium ion batteries. J Mater Chem A 2015;3(5):2036–42.

[14] Jia H, Zheng J, Song J, Luo L, Yi R, Estevez L, et al. A novel approach to synthesize micrometer-sized porous silicon as a high performance anode for lithium-ion batteries. Nano Energy 2018;50:589–97.
[15] Xiao Q, Gu M, Yang H, Li B, Zhang C, Liu Y, et al. Inward lithium-ion breathing of hierarchically porous silicon anodes. Nat Commun 2015;6(1):8844.
[16] Han X, Zhang Z, Chen S, Yang Y. Low temperature growth of graphitic carbon on porous silicon for high-capacity lithium energy storage. J Power Sources 2020;463:228245.
[17] Dou F, Weng Y, Chen G, Shi L, Liu H, Zhang D. Volume expansion restriction effects of thick TiO_2/C hybrid coatings on micro-sized SiO_x anode materials. Chem Eng J 2020;387:124106.
[18] Han J, Chen G, Yan T, Liu H, Shi L, An Z, et al. Creating graphene-like carbon layers on SiO anodes via a layer-by-layer strategy for lithium-ion battery. Chem Eng J 2018;347:273–9.
[19] Guo S, Hu X, Hou Y, Wen Z. Tunable synthesis of yolk–shell porous silicon@carbon for optimizing Si/C-based anode of lithium-ion batteries. ACS Appl Mater Interfaces 2017;9(48):42084–92.
[20] Tong L, Wang P, Fang W, Guo X, Bao W, Yang Y, et al. Interface engineering of silicon/carbon thin-film anodes for high-rate lithium-ion batteries. ACS Appl Mater Interfaces 2020;12(26):29242–52.
[21] Chen H, Ling M, Hencz L, Ling HY, Li G, Lin Z, et al. Exploring chemical, mechanical, and electrical functionalities of binders for advanced energy-storage devices. Chem Rev 2018;118(18):8936–82.
[22] Cao PF, Yang G, Li B, Zhang Y, Zhao S, Zhang S, et al. Rational design of a multifunctional binder for high-capacity silicon-based anodes. ACS Energy Lett 2019;4(5):1171–80.
[23] Yuca N, Zhao H, Song X, Dogdu MF, Yuan W, Fu Y, et al. A systematic investigation of polymer binder flexibility on the electrode performance of lithium-ion batteries. ACS Appl Mater Interfaces 2014;6(19):17111–8.
[24] Kovalenko I, Zdyrko B, Magasinski A, Hertzberg B, Milicev Z, Burtovyy R, et al. A major constituent of brown algae for use in high-capacity Li-ion batteries. Science 2011;334(6052):75–9.
[25] Ling M, Qiu J, Li S, Yan C, Kiefel MJ, Liu G, et al. Multifunctional SA-PProDOT binder for lithium ion batteries. Nano Lett 2015;15(7):4440–7.
[26] Choi S, Kwon TW, Coskun A, Choi JW. Highly elastic binders integrating polyrotaxanes for silicon microparticle anodes in lithium ion batteries. Science 2017;357(6348):279–83.
[27] Magasinski A, Zdyrko B, Kovalenko I, Hertzberg B, Burtovyy R, Huebner CF, et al. Toward efficient binders for Li-ion battery Si-based anodes: polyacrylic acid. ACS Appl Mater Interfaces 2010;2(11):3004–10.
[28] Guo R, Zhang S, Ying H, Yang W, Wang J, Han WQ. New, effective, and low-cost dual-functional binder for porous silicon anodes in lithium-ion batteries. ACS Appl Mater Interfaces 2019;11(15):14051–8.
[29] Munao D, van Erven JWM, Valvo M, Garcia-Tamayo E, Kelder EM. Role of the binder on the failure mechanism of Si nano-composite electrodes for Li-ion batteries. J Power Sources 2011;196(16):6695–702.
[30] Ling M, Xu Y, Zhao H, Gu X, Qiu J, Li S, et al. Dual-functional gum arabic binder for silicon anodes in lithium ion batteries. Nano Energy 2015;12:178–85.
[31] Song J, Zhou M, Yi R, Xu T, Gordin ML, Tang D, et al. Interpenetrated gel polymer binder for high-performance silicon anodes in lithium-ion batteries. Adv Funct Mater 2014;24(37):5904–10.
[32] Yu X, Yang H, Meng H, Sun Y, Zheng J, Ma D, et al. Three-dimensional conductive gel network as an effective binder for high-performance Si electrodes in lithium-ion batteries. ACS Appl Mater Interfaces 2015;7(29):15961–7.
[33] Liu T, Chu Q, Yan C, Zhang S, Lin Z, Lu J. Interweaving 3D network binder for high-areal-capacity Si anode through combined hard and soft polymers. Adv Energy Mater 2019;9(3):1802645.
[34] Ling M, Liu M, Zheng T, Zhang T, Liu G. Investigating the doping mechanism of pyrene based methacrylate functional conductive binder in silicon anodes for lithium-ion batteries. J Electrochem Soc 2017;164(4):A545–8.
[35] Wei D, Mao J, Zheng Z, Fang J, Luo Y, Gao X. Achieving a high loading Si anode via employing a triblock copolymer elastomer binder, metal nanowires, and a laminated conductive structure. J Mater Chem A 2018;6(42):20982–91.
[36] Xu Z, Yang J, Zhang T, Nuli Y, Wang J, Hirano S. Silicon microparticle anodes with self-healing multiple network binder. Joule 2018;2(5):950–61.
[37] Wei L, Chen C, Hou Z, Wei H. Poly (acrylic acid sodium) grafted carboxymethyl cellulose as a high performance polymer binder for silicon anode in lithium ion batteries. Sci Rep 2016;6(1):19583.
[38] Cai Y, Li Y, Jin B, Ali A, Ling M, Cheng D, et al. Dual cross-linked fluorinated binder network for high-performance silicon and silicon oxide based anodes in lithium-ion batteries. ACS Appl Mater Interfaces 2019;11(50):46800–7.
[39] Wang KL, Chen KT, Yi YH, Hung YH, Tuan HY, Horie M. High-performance lithium ion batteries combining submicron silicon and thiophene–terephthalic acid conjugated polymer binders. ACS Sustain Chem Eng 2020;8(2):1043–9.
[40] Mandal P, Stokes K, Hernández G, Brandell D, Mindemark J. Influence of binder crystallinity on the performance of Si electrodes with poly(vinyl alcohol) Binders. ACS Appl Energy Mater 2021;4(4):3008–16.
[41] Hu S, Cai Z, Huang T, Zhang H, Yu A. A modified natural polysaccharide as a high-performance binder for silicon anodes in lithium-ion batteries. ACS Appl Mater Interfaces 2019;11(4):4311–7.
[42] Tang R, Ma L, Zhang Yu, Zheng X, Shi Y, Zeng X, et al. A flexible and conductive binder with strong adhesion for high performance silicon-based lithium-ion battery anode. ChemElectroChem 2020;7(9):1992–2000.
[43] Lee HA, Shin M, Kim J, Choi JW, Lee H. Designing adaptive binders for microenvironment settings of silicon anode particles. Adv Mater 2021;33(13):2007460.
[44] Iyengar DR, Perutz SM, Dai CA, Ober CK, Kramer EJ. Surface segregation studies of fluorine-containing diblock copolymers. Macromolecules 1996;29(4):1229–34.
[45] Shimomoto H, Fukami D, Irita T, Katsukawa KI, Nagai T, Kanaoka S, et al. Synthesis of fluorine-containing star-shaped poly(vinyl ether)s via arm-linking reactions in living cationic polymerization. J Polym Sci A 2012;50(8):1547–55.
[46] Kahveci MU, Mangold C, Frey H, Yagci Y. Graft copolymers with complex polyether structures: poly(ethylene oxide)-*graft*-poly(isobutyl vinyl ether) by combination of living anionic and photoinduced cationic graft polymerization. Macromol Chem Phys 2014;215(6):566–71.
[47] Hashimoto T, Nakamura T, Tanahashi S, Kodaira T. Gel formation in cationic polymerization of divinyl ethers. III. Effect of oligooxyethylene chain versus oligomethylene chain as central spacer units. J Polym Sci A 2004;42(15):3729–38.
[48] Yonezawa N, Mori S, Miyata S, Ueha-Anyashiki Y, Maeyama K. Synthesis of aromatic poly(ether ketone)s having adhesion property to steel surface. React Funct Polym 2002;53(1):11–7.
[49] Devrim ES, Kahveci MU, Tasdelen MA, Ito K, Yagci Y. Synthesis of poly(isobutyl vinyl ether)-*graft*-poly(ethylene oxide) co-polymer with pendant methacrylate functionality and its photo-curing behavior. Des Monomers Polym 2009;12(3):265–72.
[50] Tran B, Oladeji IO, Zou J, Chai G, Zhai L. Adhesive poly(PEGMA-*co*-MMA-*co*-IBVE) copolymer electrolyte. Solid State Ion 2013;232:37–43.
[51] Oda Y, Horinouchi A, Kawaguchi D, Matsuno H, Kanaoka S, Aoshima S, et al. Effect of side-chain carbonyl groups on the interface of vinyl polymers with water. Langmuir 2014;30(5):1215–9.
[52] Liu X, Wang CG, Goto A. Polymer dispersity control by organocatalyzed living radical polymerization. Angew Chem Int Ed Engl 2019;58(17):5598–603.
[53] Kasinathan R, Marinaro M, Axmann P, Wohlfahrt-Mehrens M. Influence of the molecular weight of poly-acrylic acid binder on performance of Si-alloy/graphite composite anodes for lithium-ion batteries. Energy Technol 2018;6(11):2256–63.
[54] Hu B, Shkrob IA, Zhang S, Zhang L, Zhang J, Li Y, et al. The existence of optimal molecular weight for poly(acrylic acid) binders in silicon/graphite composite anode for lithium-ion batteries. J Power Sources 2018;378:671–6.
[55] Liu D, Xie Y, Xu R, Wang Y, He L, Yan X, et al., inventors; Dongguan Amperex Tech Ltd., Ningde Amperex Technology Ltd., assignees. Qualitative analysis method for adhesive property of adhesive. China patent CN102323249A. 2012 Jan 18. Chinese.